



Dynamic necking of a near α titanium alloy at high strain rates: Experiments and modelling

Long-hui Zhang, Antonio Pellegrino^{*}, Nik Petrinic

Department of Engineering Science, University of Oxford, Oxford, OX1 3PJ, UK

ARTICLE INFO

Article history:

Received 10 February 2020

Received in revised form

10 May 2020

Accepted 2 July 2020

Available online 9 July 2020

Keywords:

Near α titanium alloy

High strain rate

Locking effect

Constitutive modeling

Finite element simulation

ABSTRACT

The tensile behaviour of near α Ti3Al2.5 V alloy, conceived for applications in aerospace and automotive engineering, is characterized from quasi-static to high strain rates. The material is found to present noticeable strain rate sensitivity. The dynamic true strain rate in the necking cross-section reaches values up to ten times higher than the nominal strain rate. It is also observed that beyond necking the dynamic true stress-strain curves present limited rate dependence. The experimental results at different strain rates are used to determine a suitable constitutive model for finite element simulations of the dynamic tensile tests. The model predicts the experimentally macroscopic force-time response, true stress-strain response and effective strain rate evolution with good agreement.

© 2020 China Ordnance Society. Publishing services by Elsevier B.V. on behalf of KeAi Communications Co. Ltd. This is an open access article under the CC BY-NC-ND license (<http://creativecommons.org/licenses/by-nc-nd/4.0/>).

1. Introduction

Metals employed in automatable and aeronautical applications are often undergoing high-speed deformation process. The dynamic tensile behaviour of metals has been popularly characterized by means of the Split Hopkinson Tension Bar apparatus (SHTB) since Harding et al. [1]. However, the interpretation of this experiment is subjected to non-uniform deformations and dynamic necking localization. To improve the accuracy of the dynamic measurement, the SHTB with high-speed image recording can provide the real time information of the tensile deformation and the necking localization, as reported by Noble et al. [2] and Mirone [3]. As a non-contact optical technique, Digital Image Correlation (DIC) is a popular full-field strain measurement technique. Qin et al. [4] reported the strain evolution of the dual-phase high strength steel specimens and Tzibula et al. [5] examined the dynamic stress and strain evolutions in polymers using high speed DIC technique. Sato et al. [6] employed the DIC technique to determine dynamic response at large strains by determining the true stress–strain data in the necked zone.

Titanium alloys with high strength-to-weight ratio are widely

used in aerospace, automotive, and other industrial fields. In aeronautic industry, titanium alloys serve as structural components such as turbine fan blades and engine containment components and are usually designed to be subjected to dynamic loading. Meyers et al. [7] studied the temperature and strain rate sensitivity of commercially pure α titanium at high strain rates. Chichili et al. reported the dynamic compression response of pure α titanium with pronounced strain hardening and substantial strain rate dependent flow stress. Lee and Lin [8] investigated the high rate plastic deformation of Ti6Al4V alloy under various temperature conditions, and found that the temperature sensitivity was independent of strain rate but increased with increasing temperature, and the shear bands were the precursor to final fracture. Macdougall and Harding [9] studied adiabatic temperature rise in Ti6Al4V during dynamic torsion and tension tests at high strain rates and calibrated the strain rate and temperature dependent constitutive model. Wielewski et al. [10] investigated the effects of strain rate, crystallographic texture and direction of loading on the macroscopic stress–strain response of Ti6Al4V by using the Hopkinson bars and the high speed DIC techniques. Titanium alloys deforming at high strain rate are very prone to fail by strain localization. In terms of shear localization, Zhang et al. [11] reported the adiabatic heating and dynamic shear failure of structural titanium alloys such as Ti3Al2.5 V alloy. However, studies about dynamic necking localization of Ti3Al2.5 V alloy are still limited. Recently, Mirone et al. [12] pointed out the strain rate locking effect

^{*} Corresponding author.

E-mail address: antonio.pellegrino@eng.ox.ac.uk (A. Pellegrino).

Peer review under responsibility of China Ordnance Society

in a mild steel, in which the dynamic amplification stopped to increase and remained locked to the value at the onset of necking, in spite of uncontrollable rise of the effective strain rate beyond necking. However, the interaction between the onset of necking and the effective strain rate influence on the flow stress has not been reported for a titanium alloy. In the present paper, dynamic tensile experiments, complemented by high speed imaging, are conducted to measure the engineering and true stress-strain response, as well as the effective strain rate evolution beyond dynamic necking of a near α Ti3Al2.5 V alloy. This alloy was selected as a model material used in the aeronautic industry due to its good cold formability combined with its excellent strength-to-weight ratio. The experimental measurement of local strain and strain rate during dynamic necking will provide the guidance for the design of impact containment applications.

The present work aims at studying the strain rate (and temperature) dependent constitutive response of the near α Ti3Al2.5 V alloy and at investigating the strain and strain rate evolutions inside the neck, in order to check whether there is a dynamic strain rate locking effect. In this paper, the materials and experimental setups are introduced in Section 2. The experimental results at low and high strain rates are presented in Section 3. The following section describes the constitutive model and the numerical simulations of the tensile experiments at high strain rates. The main outcome of the work is discussed in Section 5, following by conclusions.

2. Material and methods

2.1. Material and specimens

The Grade 9 Ti3Al2.5 V alloy, supplied as 10 mm diameter rod, was subjected to microstructural characterization for revealing the as-received initial microstructure. The specimen was prepared following standard procedure including polishing with 0.04 μm silica particles, and etched by Kroll etchant. Fig. 1 shows an equiaxed α microstructure with an average grain size of about 6 μm . Table 1 gives the chemical compositions. Two specimen geometries with the gauge length to diameter ratio 8 mm–3mm and 3 mm–3mm are used to obtain wide ranges of strain rates. The dimensions of the specimens are shown in Fig. 2. The tensile specimens were machined along the axis direction from the as-received rod, with the surface roughness Ra0.25 in the gauge section.

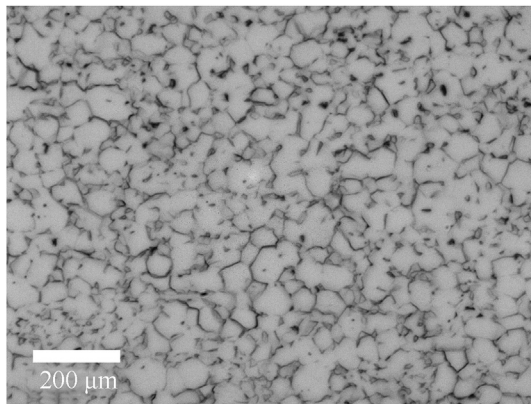


Fig. 1. Initial microstructure of Ti3Al2.5 V investigated.

Table 1
Chemical composition of Ti3Al2.5 V (wt%).

Ti	Al	V	O	Fe	N	C	H	Mo
Balanced	3	2.5	0.15	0.25	0.03	0.08	0.015	0

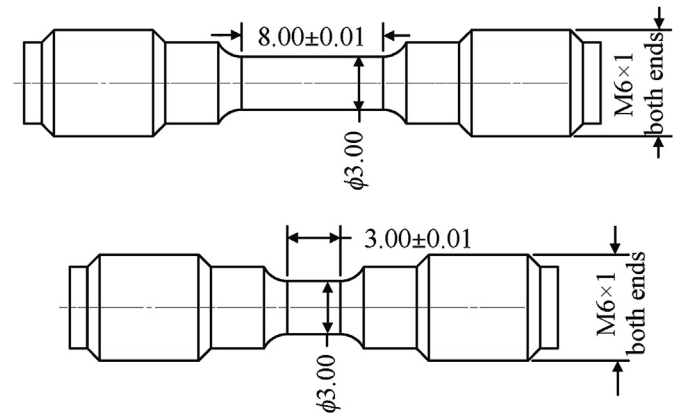


Fig. 2. Geometry and dimensions of the short and long gage specimen (All dimensions in mm).

2.2. Methods

The tensile experiments at quasi-static condition were carried out using a 50 kN screw-driven Zwick machine under displacement control synchronized with a high definition camera. LaVision Davis¹ software was employed for the strain measurements of specimen gauge section via analysis of the deformation images.

The tensile experiments at high rates were conducted using a recently designed 10 mm diameter Kolsky tension bar (Fig. 3) reported by Gerlach et al. [13]. The incident bar was made of Ti6Al4V alloy while the output bar was made of phosphor bronze, both were of length equal to 2.7 m. The striker bar was made of Ti6Al4V alloy with a length 0.5 m. Several high rate tensile rate tests at 100 °C and 200 °C were also performed by using the induction heater to evaluate temperature effect on the mechanical behaviour. To monitor the temperature during heating, a K-type thermocouple was spot welded on the centre surface of the specimen. When the temperature reached the target temperatures with ± 5 °C error and was stable for 1 min, the striker bar was fired. All experiments were recorded using the ultra-high speed Kirana camera.²

Two strain gage bridges are attached on the input bar and one strain gage bridge is attached on the output bar. An in-house developed algorithm is employed to separate the incident and reflected wave and, in turn, determining the velocities and forces at the interface between the bars and the specimen. The stress and strain histories are obtained by the classical Kolsky bar analysis [14]. In Fig. 4, the amplitude of travelling waves histories at the interfaces between the tensile specimen and the Kolsky bars is determined by the D'Alambert's solution of wave equations, which can be found in detail in Refs. [15]. A summary of the experiments conducted at low and high rates are given in Table 2. Typical strain gage signals are shown in Fig. 5.

¹ LaVisionUK Ltd, 2 Minton Place Victoria Road, Bicester OX26 6QB, United Kingdom.

² Specialised Imaging Ltd, UK.

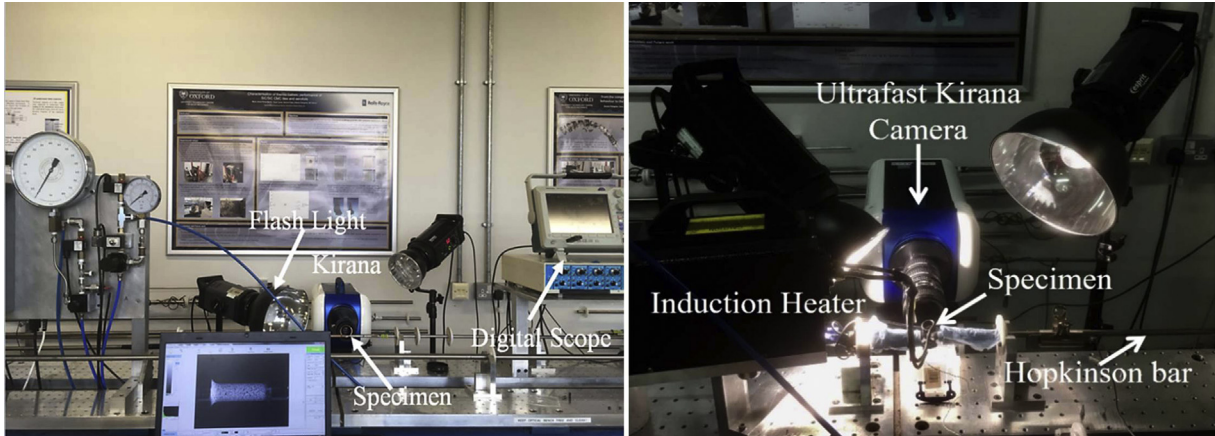


Fig. 3. Experimental Setup-SHTB System with kirana camera.

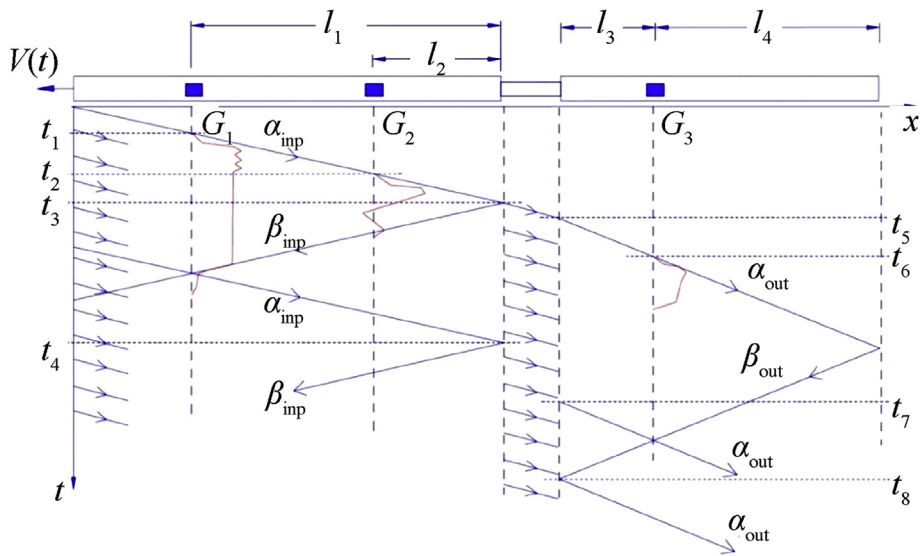


Fig. 4. Wave propagation analysis.

3. Experimental results

3.1. Quasi-static experimental results

Fig. 6a shows the engineering stress-strain curves under quasi-static condition. True strain and true stress data based on Bridgman analysis [16,17] were calculated as follows:

Table 2
Summary of the tested tensile specimens and the corresponding nominal strain rates.

Length to Diameter Ratio	Strain rate/(s ⁻¹)	Number of Tests	Condition
8–3	0.001	3	25 °C
		4	25 °C
		2	100 °C
		1	200 °C
		2	25 °C
3–3	2400	2	25 °C
	1600	1	25 °C
	2700	2	25 °C

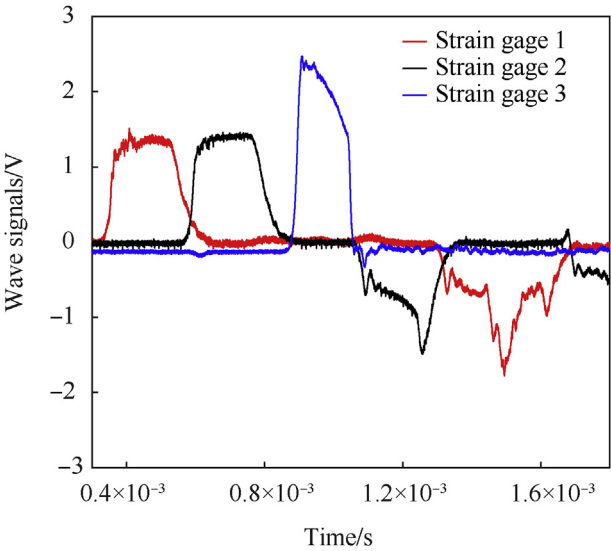


Fig. 5. Typical raw strain gage signals at strain rate of ~2400 s⁻¹.

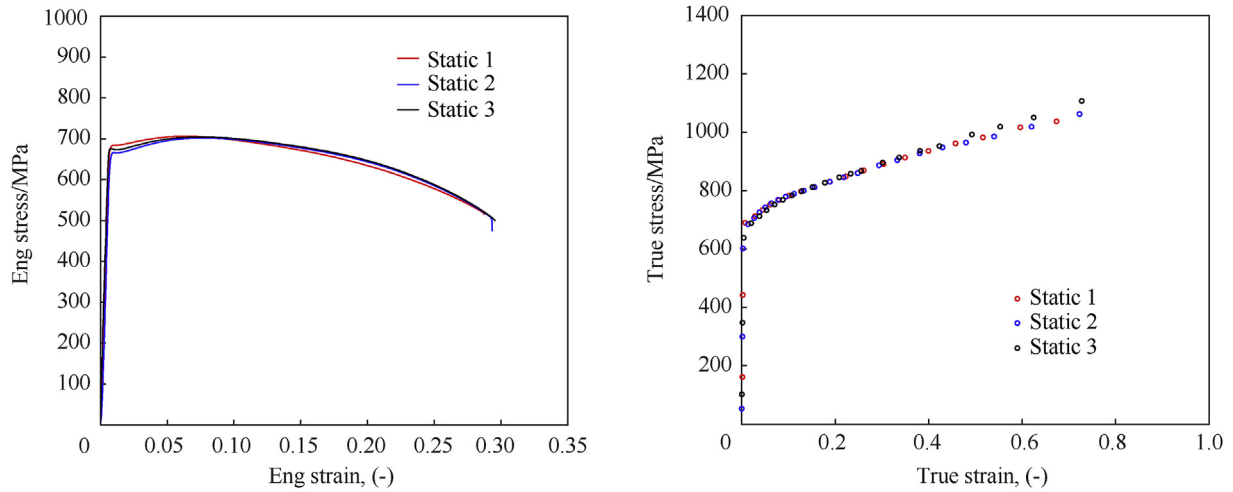


Fig. 6. Quasi-static stress-strain curves of Ti3Al2.5 V alloy.

$$\varepsilon_{\text{true}} = 2 \cdot \ln\left(\frac{r_0}{r}\right) \quad (1)$$

$$\sigma_{\text{true}} = \frac{F}{\pi \cdot r^2} \quad (2)$$

Here, r_0 and r express the initial and the current radius of the minimum cross section. F is the instantaneous acting force. The image analysis yields the true strain data. The true stress-strain curves are presented in Fig. 6b. The average ultimate engineering stress is 703 MPa, with the engineering strain to failure approximately 29%. The average maximum true stress value is equal to 1072 MPa and the average true strain to failure is 71%.

3.2. High rate experimental results

Fig. 7 shows typical DIC images for long and short gauge length specimens at 2400–2700 s^{-1} . The engineering strain of the specimen is measured from the elongation of the mid-section line. Most of gauge section in short gauge length specimen undergoes localization, which is not the case for long gauge length specimen.

The comparison of true strain and engineering strain histories in Fig. 8 clearly shows that the dynamic true failure strain is in the region of 0.48, which is completely different from the geometry (and strain rate) dependent engineering failure strain. The dynamic engineering stress-strain curves and true stress-strain curves are compared in Fig. 9. The short gauge length specimens show

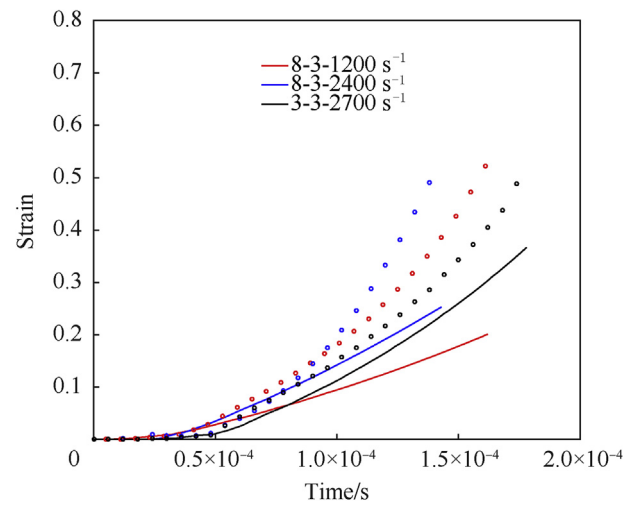


Fig. 8. True strain and engineering strain as a function of time at high strain rates.

engineering failure strains about 34%, which are higher than those from long gauge length specimens, indicating that after the onset of necking, the engineering strain is influenced by the specimen geometry, rather than a real property of the Ti3Al2.5 V alloy itself. However, the true stress-true strain curves are found to be independent of the specimen geometry. Dynamic true stress-strain

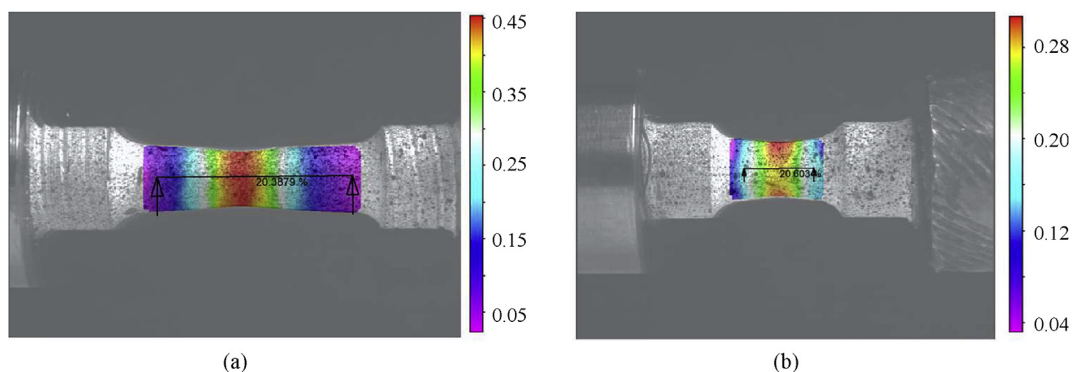


Fig. 7. Typical DIC images for long and short gauge length specimens at 2400–2700 s^{-1} . The axis engineering strain is shown.

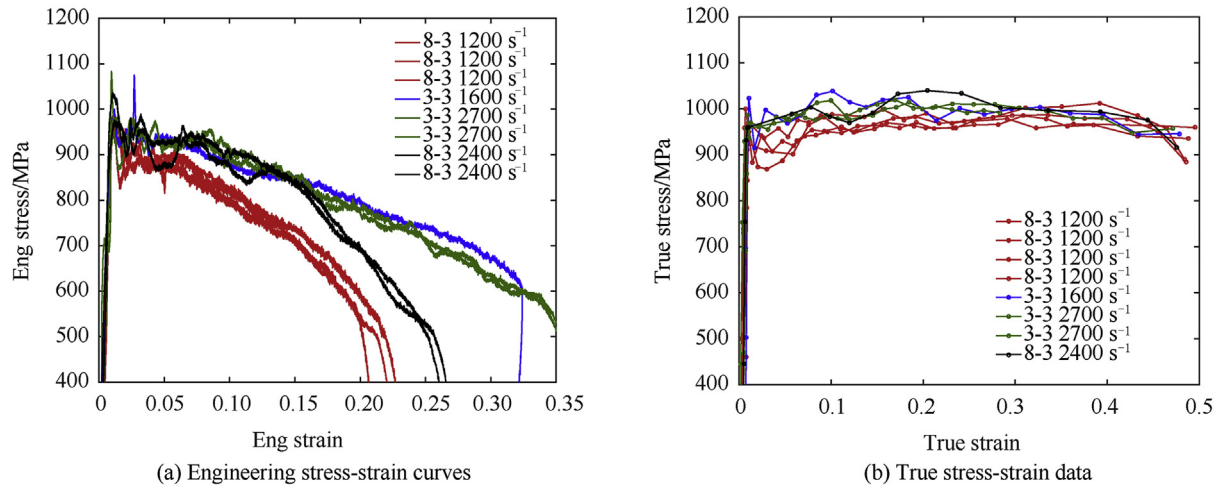


Fig. 9. Comparisons of the high rate tensile stress-strain curves.

curves at 2400–2700 s^{-1} are only slightly higher than those obtained at 1200 s^{-1} .

Additional high rate tensile rate tests at 100 °C and 200 °C were also performed by using a suitable induction heater installed on the Hopkinson bar, to evaluate temperature effects on the mechanical behaviour. The engineering stress-strain curves at 1200 s^{-1} at 25 °C, at 100 °C and 200 °C are shown in Fig. 10. With the increase of the temperature, the flow stress decreases, while the engineering strain to failure increases.

The true strain rate can be determined experimentally as: $\dot{\epsilon}_{\text{true}} = \frac{d}{dt} \left[2 \cdot \ln \left(\frac{r_0}{r} \right) \right]$, where r_0 and r are the initial and current diameter of the minimum cross-section of the specimen measured by means of high speed photography. Fig. 11 examines the true strain rate evolution during tensile deformation and shows the true strain rate increases continuously until failure, up to approximately 10000 s^{-1} , which is ten times higher than the nominal strain rate. The short gage specimen exhibits smaller true strain rate at a given true strain under same imposed nominal strain rate loading condition. The nominal strain rate is found to significantly underestimate the effective strain rate beyond necking and could be misleading when characterising the dynamic constitutive response of ductile alloys.

The typical microstructures of Ti3Al2.5 V were examined using

optical microscopy. The loading direction is marked in the images. Fig. 12a shows the deformed microstructure adjacent to the fracture surface of a specimen tested quasi statically. Fig. 12b presents the microstructure a nominal strain rate equal to 1200 s^{-1} . Compared to the initial equiaxed microstructure, the grains elongate significantly towards the loading direction. Fig. 12c shows an adiabatic shear band (ASB) with cracks (dashed circles) in the fractured gauge section for a specimen tested at a nominal strain rate equal to 2400 s^{-1} , typical characteristic of ductile failure at high strain rates, which is in agreement with the macro measured very high effective strain rate in the necking zone.

4. Constitutive modelling and numerical simulation

4.1. Constitutive modelling

The dynamic mechanical responses of metallic alloys are widely described by the Johnson-Cook (JC) [18] model and the Khan–Huang–Liang (KHL) [19,20] model. Taking into account the present experimental condition, and the stress-strain response of the Ti3Al2.5 V alloy, both of the advantages of JC and KHL model are

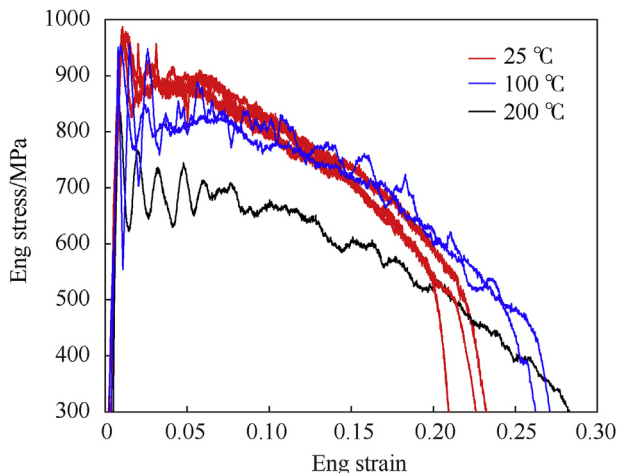


Fig. 10. High rate stress-strain curves under room temperature, 100 °C and 200 °C temperature.

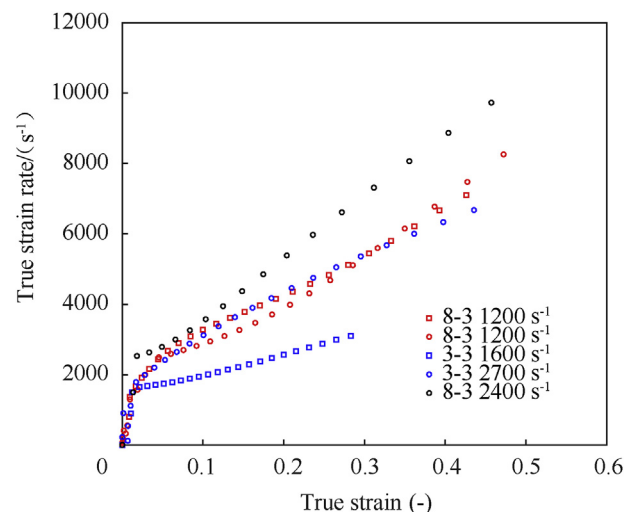


Fig. 11. Typical true strain rate evolution during high rate tensile experiments at room temperature.

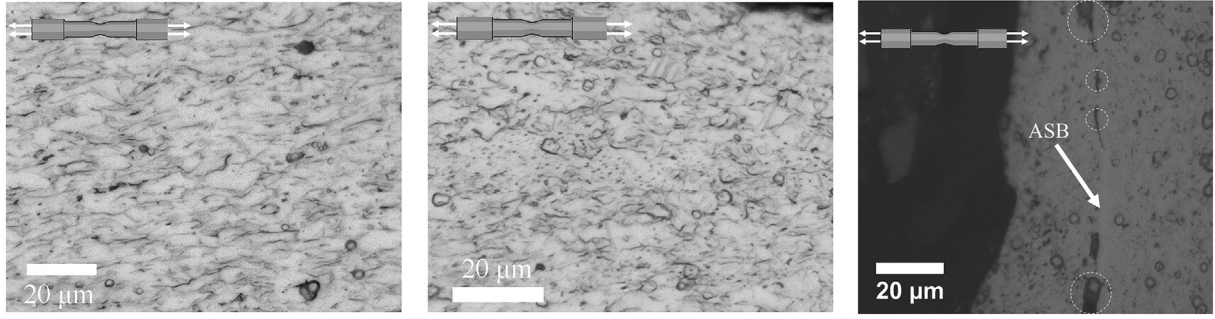


Fig. 12. Micrograph of highly deformed Ti3Al2.5 V specimens (a) quasi-static (b) 1200 s⁻¹ (c) 2400 s⁻¹.

employed, which shows the decreasing strain hardening with strain rate, and logarithmic strain rate dependent flow stress, with the reference strain rate 0.001 s⁻¹. Here, the combined JC-KHL model (CJK) is proposed to describe the constitutive response of Ti3Al2.5 V. The present CJK model is as follows,

$$\sigma = \left[A + B \left(1 - \frac{\ln\left(\frac{\dot{\epsilon}}{\dot{\epsilon}_0}\right)}{\ln D_0^p} \right)^{n_1} (\epsilon_p)^{n_0} \right] \left(1 + C \ln \left(\left(\frac{\dot{\epsilon}}{\dot{\epsilon}_0} \right) \right) \right) \left(\frac{T_m - T}{T_m - T_r} \right)^m \quad (3)$$

Here, σ is the true stress, ϵ_p is the plastic strain, $\dot{\epsilon}_0$ is a reference strain rate and D_0^p is an upper bound strain rate chosen arbitrarily. The constants are A , B , C , m , n_1 and n_0 . T , T_r and T_m , are current, reference and melting temperatures.

Due to the conversion of plastic work into heat, the deformation of titanium alloys at high strain rates is associated with an adiabatic temperature rise. The integration of the transient stress-thermal balance equation with the neglect of thermoelastic couplings, under adiabatic conditions, results in:

$$\beta_{\text{int}} \int_0^{\alpha} \sigma d\epsilon_p = \rho c_p \Delta T \quad (4)$$

where β_{int} is the Taylor-Quinney coefficient [21], namely, the portion of the plastic energy dissipated to heat. ρ is the density, c_p is the specific heat capacity and ΔT is the temperature rise. Here, the Density 4500 (kg/m³), Specific heat 526 (J/kg·K), Young modulus 110 GPa, Poisson Ratio 0.33, Melting temperature 1705 °C, and β_{int} factor 0.55 [11,21,22], typical for titanium alloys, are chosen as the properties of Ti3Al2.5 V.

At the reference strain rate of 0.001 s⁻¹, Eq. (3) reduces to $\sigma = A + B(\epsilon_p)^{n_0}$. The average quasi-static curve yields the parameters $A = 620$ MPa, $B = 341$ MPa and $n_0 = 0.35$, by using the method of least squares in the curve fitting tool in MATLAB.

High rate experiments at strain rate 1200 s⁻¹ at 100 °C and 200 °C temperatures are used to determine the thermal softening parameter m . Adiabatic heating is not considered when calibrating the material constants, because the experimentally measured temperature rise remains quite modest, not exceeding 9 °C, according to the recently reported engineering stress-strain-temperature of the titanium alloys at strain rate of 1500 s⁻¹ [22]. At the same nominal strain rate of 1200 s⁻¹, the ratios R_{100} between the stresses at 100 °C and 25 °C, and R_{200} between the stresses at 200 °C and 25 °C at a specific plastic strain are $R_{100} =$

$\frac{\sigma_{100}}{\sigma_{25}} = \left(\frac{T_m - 100}{T_m - T_r} \right)^m$ and $R_{200} = \frac{\sigma_{200}}{\sigma_{25}} = \left(\frac{T_m - 200}{T_m - T_r} \right)^m$. The stress values in

Fig. 13a at 100 °C and 200 °C are divided by the stress values at room temperature 25 °C. Fig. 13b shows that the averaged values are $R_{100} = 0.9131$, and $R_{200} = 0.7766$ respectively, resulting in $m = 1.98$ at 100 °C and $m = 2.30$ at 200 °C. An average value of $m = 2.14$ is adopted.

When $\epsilon_p = 0$, Eq. (3) reduces to $\sigma = A \left(1 + C \ln \left(\left(\frac{\dot{\epsilon}}{\dot{\epsilon}_0} \right) \right) \right)$. The constant $C = 0.0365$ is calculated interpolating the dynamic yield stress values. $D_0^p = 10^{22}$ s⁻¹ is an upper bound strain rate chosen arbitrarily, given that the strain rate in the present work cannot exceed 10²² s⁻¹. The constant n_1 is determined interpolating the dynamic stress-strain curves, with an average value $n_1 = 100$. The calibrated CJK constitutive model for Ti3Al2.5 V is therefore as follows,

$$\sigma = \left[620 + 341 \left(1 - \frac{\ln\left(\frac{\dot{\epsilon}}{\dot{\epsilon}_0}\right)}{\ln D_0^p} \right)^{100} (\epsilon_p)^{0.35} \right] \left(1 + 0.0365 \ln \left(\left(\frac{\dot{\epsilon}}{\dot{\epsilon}_0} \right) \right) \right) \left(\frac{T_m - T}{T_m - T_r} \right)^{2.14} \quad (5)$$

The calibrated model is compared to the experimental quasi-static and dynamic true stress–plastic curves data in Fig. 14, with the error $\left| \frac{\sigma_{\text{exp}} - \sigma_{\text{model}}}{\sigma_{\text{exp}}} \right| \times 100\%$ less than 8%. Table 3 summarises the obtained model parameters. The constitutive model prediction is compared to the experimental measurements in section 4.2.

4.2. Numerical simulations

The numerical simulations are conducted by using ABAQUS [23] to evaluate the CJK prediction compared to the experimental measurements.

4.2.1. Finite element model

To reduce the computational time cost, only half of the specimen is modelled without the threads. The specimen is meshed with three-dimensional linear hexahedral elements with hourglass control (reduced integration element C3D8R). The elements have an initial aspect ratio 1:1:1 with dimensions 0.1 × 0.1 × 0.1 mm³ for the specimen gage section. The boundary conditions at the two end faces are the experimental recorded incident and transmitted velocities. In addition to the constitutive model described above, the present simulation adopts a simple failure criterion which allows elements to be removed from the mesh when the equivalent strain exceeds a critical strain, reported by Macdougall and Harding [9]. Specifically, once the critical strain value is reached the element

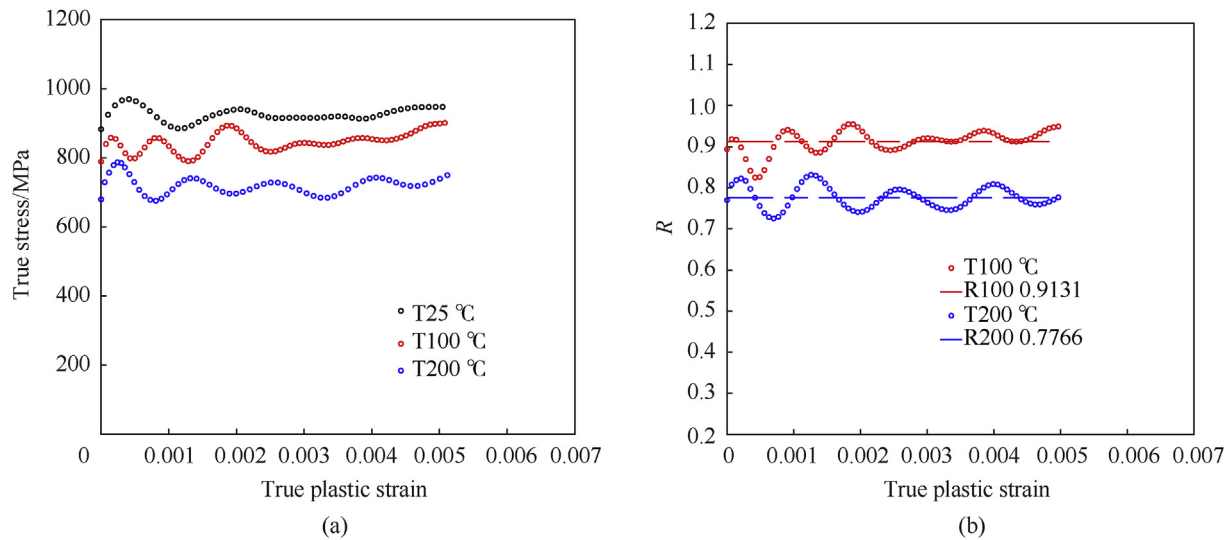


Fig. 13. High rate experimental results for the evaluation of thermal softening. (a) experimental curves at temperatures: 25 °C, 100 °C and 200 °C. (b) ratios between stress values at 100 °C and 200 °C to stress values at 25 °C and their average value R .

linearly reduces its strength until its stress bearing capability is completely lost and is then removed. Here, the equivalent strain $\varepsilon_{cr} = 0.48$ is used as the critical strain failure criterion. After the critical plastic strain is exceeded, the element loses its strength in a linear manner until final fracture. The CJK model and the simple damage model are implemented into ABAQUS by means of a VUMAT subroutine using the radial return algorithm introduced in detail in Ref. [24].

4.2.2. Simulation results

The numerical force-time histories at strain rates of 1200 s^{-1} and 2400 s^{-1} at room temperature are compared to the experimental data in Fig. 15. The force in numerical simulation, which is the total reaction force from the specimens end face, match well with the experimental data, indicating the capability of the proposed rate and temperature dependent constitutive model to describe the tensile behaviour of the near α Ti3Al2.5 V alloy at high strain rates.

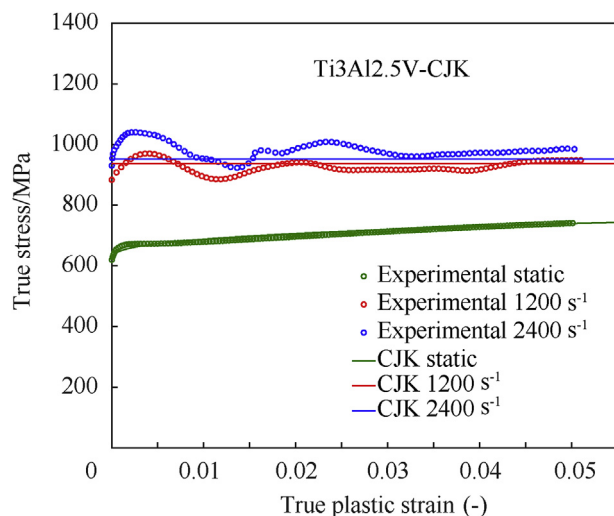


Fig. 14. Comparison between the constitutive model description and the experimental true stress-true plastic strain curves.

Fig. 16 compares the experimental and numerical true stress-strain data and true strain rate histories. The true stress-strain curves from the simulation are in good agreement with the experimental data. The numerical true stress-strain curves are the average axial stress-strain values from the elements located at the current minimum cross-section. Due to the necking localization, the true strain rate reaches values up to ten times higher than the nominal strain rate. The numerical and experimental true strain rate histories are also in excellent agreement.

5. Discussion

This paper studies the tensile behaviour of a near α Ti3Al2.5 V alloy from quasi-static to high strain rates, with particular emphasis on revealing whether there is any locking effect on the rate dependence of a titanium alloy. After the onset of necking, the engineering strain is affected by the specimen geometry, rather than being a property of the material itself. However, the true stress-true strain curves are found to be independent of the specimen geometry. The elongation based dynamic engineering stress-strain characteristics are compared to the specimen diameter evolution based true stress-strain measurements with the assistance of the ultra-high speed camera. The comparison of true strain and engineering strain histories are compared in Fig. 8, which clearly shows the true failure strain in the neck can be constant, regardless of the specimen's geometries under the strain rate region investigated in the present work. Hence, the local true failure strain is more accurate than the engineering failure strain which is influenced by the specimen's dimensions. Similar claims were made by Osovski et al. [25] that this constant local failure strain can be contrasted with the geometry dependent structural strain.

From quasi-static to high strain rate, Ti3Al2.5 V exhibits apparent strain rate sensitivity. The dynamic true stress-strain

Table 3
Summary of the CJK constitutive model parameters.

Material	CJK Constitutive Model					
	AMPa	BMPa	C	n_0	n_1	m
Ti3Al2.5 V	620	341	0.0365	0.35	100	2.14

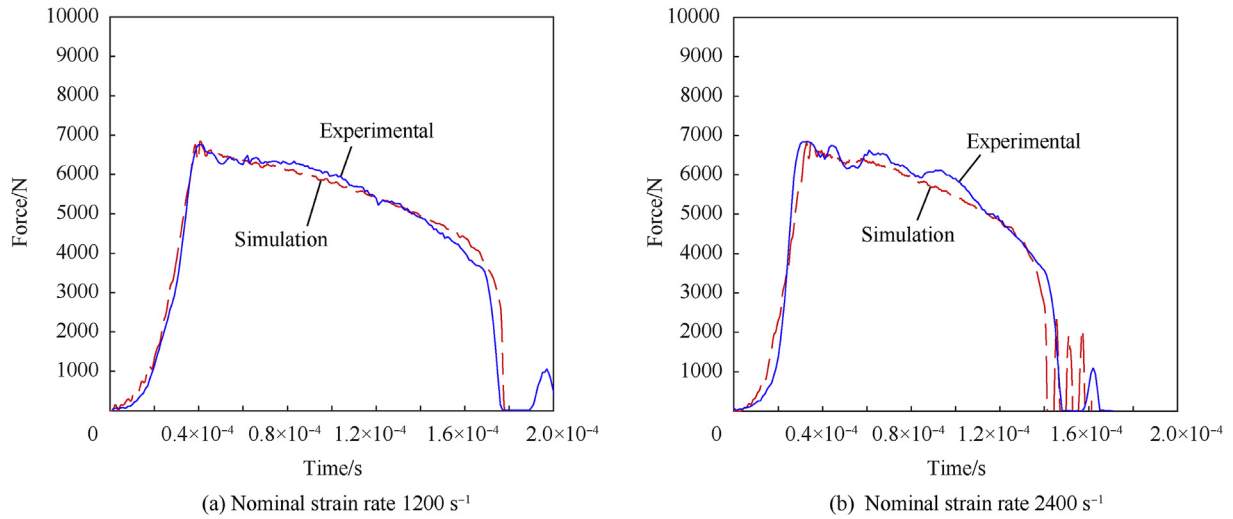


Fig. 15. Comparison between the numerical and experimental force histories.

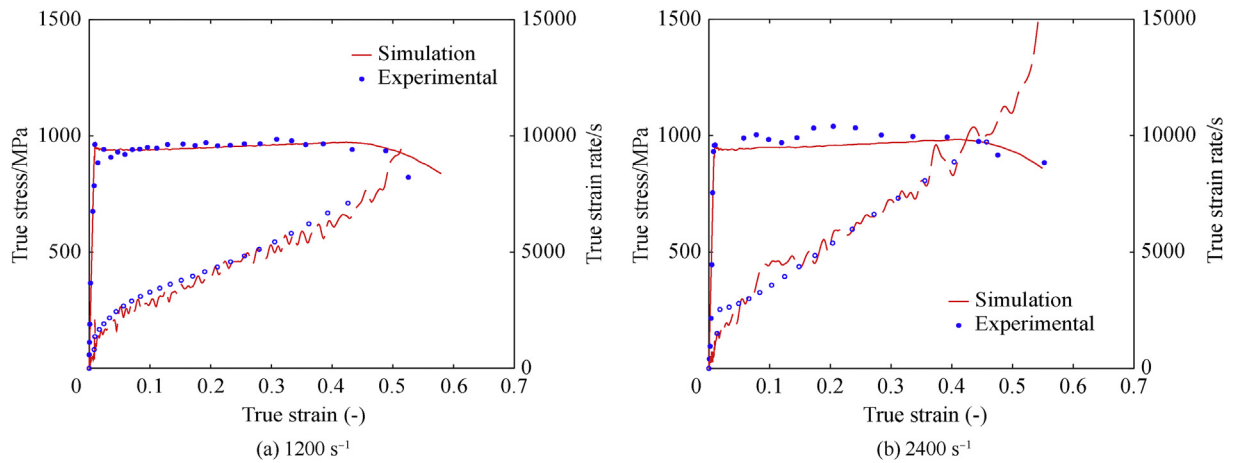


Fig. 16. Numerical true stress-strain data and the corresponding true strain rate histories with respect to the experimental measurements.

curves don't present noticeable rate dependent response, in agreement with the findings reported by Mirone et al. [12]. The true stress-strain curves of mild steel [12] with noticeable strain hardening show the strain rate locking effect, while the Ti3Al2.5 V alloy presents low strain hardening, and this strain hardening capability decreases from low to high rates. The microstructure examination clearly shows the deformed microstructures of Ti3Al2.5 V without apparently dense twins, which could contribute to the low strain hardening capacity in the stress-strain curves. The micrographs show that Ti3Al2.5 V fails by adiabatic shear band at high strain rate, typical characteristic of ductile failure mode, which is in agreement with the macro measured very high effective strain rate in the necking zone.

The suitability of the rate and temperature dependent constitutive model is evaluated via finite element simulations in ABAQUS. The numerical force-time history, true stress-strain data and the corresponding true strain rate histories are compared with the experimental results. Beyond necking, the measured true strain rate is reaching up to ten times higher than the nominal strain rate, indicating that the striker velocity can only control the effective strain rate up to necking. Further work will systematically study the temperature dependent effective strain rate evolution of the near α Ti3Al2.5 V alloy.

6. Conclusions

This paper reports the necking evolution of a near α Ti3Al2.5 V at high strain rates. The experimental measurements and the proposed constitutive model can be employed for impact containment applications.

- The mechanical response at high strain rates is different in terms of strain hardening, flow stress and failure behaviour compared to that under quasi-static condition. Ti3Al2.5 V exhibits significant strain rate sensitivity.
- The tensile engineering strain is influenced by the dimensions of the specimen, instead of a property of the Ti3Al2.5 V alloy itself.
- The analysis of the necking area allows the determination of the effective strain rate due to the necking, while the nominal strain rate in the specimens is much lower. The dynamic true stress-strain curves present limited strain rate effect beyond necking.
- The CJK model predicts the macroscopic force-time history, true strain rate evolution and true stress-strain data with good agreement compared to the experimental measurements, indicating the suitability of the proposed rate and temperature dependent constitutive model to predict of the dynamic tensile behaviour of the near α Ti3Al2.5 V alloy.

Declaration of competing interest

The authors declare that they have no known competing financial interests or personal relationships that could have appeared to influence the work reported in this paper.

Acknowledgements

The authors thank Mr. Jeffrey Fullerton, Mr. Stuart Carter, Dr David Townsend, Mrs. Karen Bamford for their assistance.

References

- [1] Harding J, Wood E, Campbell J. *J Mech Eng Sci* 1960;2:88–96.
- [2] Noble J, Goldthorpe B, Church P, Harding J. *J Mech Phys Solid* 1999;47: 1187–206.
- [3] Mirone G. *Mech Mater* 2013;58:84–96.
- [4] Qin J, Chen R, Wen X, Lin Y, Liang M, Lu F. *Mater Sci Eng, A* 2013;586:62–70.
- [5] Tzibula S, Lovinger Z, Rittel D. *Mech Mater* 2018;123:30–42.
- [6] Sato K, Yu Q, Hiramoto J, Urabe T, Yoshitake A. *Int J Impact Eng* 2015;75: 11–26.
- [7] Meyers MA, Subhash G, Kad BK, Prasad L. *Mech Mater* 1994;17:175–93.
- [8] Lee W-S, Lin C-F. *Mater Sci Eng, A* 1998;241:48–59.
- [9] Macdougall D, Harding J. *J Mech Phys Solid* 1999;47:1157–85.
- [10] Wielewski E, Arthington M, Siviour C, Petrinic N. *J Dynam Behav Mater* 2015;1:462–71.
- [11] Zhang Longhui, Rittel Daniel, Osovski S. *Mater Sci Eng, A* 2018;729:94–101.
- [12] Mirone G, Barbagallo R, Giudice F. *Int J Impact Eng* 2019;130:97–112.
- [13] Gerlach R, Kettenbeil C, Petrinic N. *Int J Impact Eng* 2012;50:63–7.
- [14] Gray III G, Blumenthal WR. *ASM handbook* 2000;8:488–96.
- [15] De Cola F, Pellegrino A, Glöckner C, Penumadu D, Petrinic N. *Exp Mech* 2018;58:223–42.
- [16] Bridgman PW. *Studies in large plastic flow and fracture*. Harvard University Press; 2013.
- [17] Mirone G. *Int J Solid Struct* 2004;41:3545–64.
- [18] Johnson GR, Cook WH. *Eng Fract Mech* 1985;21:31–48.
- [19] Khan AS, Sung Suh Y, Kazmi R. *Int J Plast* 2004;20:2233–48.
- [20] Khan AS, Kazmi R, Farrokh B. *Int J Plast* 2007;23:931–50.
- [21] Rittel D. *Mech Mater* 1999;31:131–9.
- [22] Rittel D, Zhang LH, Osovski S. *J Mech Phys Solid* 2017;107:96–114.
- [23] Abaqus V. Dassault systemes simulia corporation. 2014. p. 651.
- [24] Dunne F, Petrinic N. *Introduction to computational plasticity*. 2005.
- [25] Osovski S, Rittel D, Rodríguez-Martínez JA, Zaera R. *Mech Mater* 2013;62: 1–13.